Sciencexpress Reports

Bright and Dark Polar Deposits on Mercury: Evidence for Surface Volatiles

Gregory A. Neumann,[1]* John F. Cavanaugh,[1] Xiaoli Sun,[1] Erwan M. Mazarico,[2] David E. Smith,[2] Maria T. Zuber,[2] Dandan Mao,[3] David A. Paige,[4] Sean C. Solomon,[5,6] Carolyn M. Ernst,[7] Olivier S. Barnouin[7]

[1]NASA Goddard Space Flight Center, Code 698, Greenbelt, MD 20771, USA. [2]Department of Earth, Atmospheric and Planetary Sciences, Massachusetts Institute of Technology, Cambridge, MA 02139, USA. [3]Sigma Space Corporation, Lanham, MD 20706, USA. [4]Department of Earth and Space Sciences, University of California, Los Angeles, CA 90095, USA. [5]Department of Terrestrial Magnetism, Carnegie Institution of Washington, Washington, DC 20015, USA. [6]Lamont-Doherty Earth Observatory, Columbia University, Palisades, NY 10964, USA. [7]The Johns Hopkins Applied Physics Laboratory, Laurel, MD 20723, USA.

*To whom correspondence should be addressed. E-mail: Gregory.A.Neumann@nasa.gov

Measurements of surface reflectance of permanently shadowed areas near Mercury's north pole reveal regions of anomalously dark and bright deposits at 1064 nm wavelength. These reflectance anomalies are concentrated on poleward-facing slopes and are spatially collocated with areas of high radar backscatter postulated to be the result of near-surface water ice. Correlation of observed reflectance with modeled temperatures indicates that the optically bright regions are consistent with surface water ice, whereas dark regions are consistent with a surface layer of complex organic material that likely overlies buried ice and provides thermal insulation. Impacts of comets or volatile-rich asteroids could have provided both the dark and bright deposits.

Mercury's near-zero obliquity and impact-roughened topography (*1*) prevent direct sunlight from reaching substantial portions of its polar regions. Lacking major convective or conductive sources of heat, the permanently shadowed, near-surface regolith experiences temperatures similar to those of the icy Galilean satellites (*2*). It has long been believed on theoretical grounds that such conditions are favorable to the accumulation of volatiles (*3*, *4*). Even with Mercury's close proximity to the Sun, extremes of daytime temperature are not expected to allow surface heat to penetrate regolith to substantial depth, allowing near-surface water ice, if present, to remain stable against sublimation for billions of years (*2*). Such hypotheses were renewed when Earth-based radar observations of Mercury, at wavelengths from 3.6 to 70 cm (*5*–*9*), revealed regions of high backscatter and depolarization at both poles. Radar observations suggested that deposits of nearly pure water ice up to several meters thick lie at or near the surface. Analysis of altimetry and roughness measurements from the Mercury Laser Altimeter (MLA) (*10*, *11*) on the MErcury Surface, Space ENvironment, GEochemistry, and Ranging (MESSENGER) spacecraft (*12*) indicates that craters hosting radar-bright deposits at high northern latitudes are not anomalously shallow, nor do they display distinctive roughness properties in comparison with craters that lack such deposits (*13*). Consequently, the radar-bright material does not form a thick layer overlying regolith (*13*). A thinner surficial layer containing substantial concentrations of ice would, however, be optically brighter than the surrounding terrain (*14*) and should be detectable by active remote sensing.

We report here measurements with MLA of surface reflectance in permanently shadowed north polar regions of Mercury. The MLA instrument illuminates surface spots 20–80 m in diameter at 350–450-m intervals (*10*). The receiver system measures threshold-crossing times of the received pulse waveforms at two voltages (*15*). A single low-threshold crossing provides surface elevation, and the timing of the rising and falling signal levels for strong returns at both low and high thresholds enables MLA to estimate the received pulse energy and make active measurements of surface reflectance r_s via the lidar link equation (*16*, *17*) and preflight sensor calibrations (*10*).

During its primary mapping mission, MESSENGER orbited Mercury in an eccentric orbit with a 12-hour period and a ~200–400-km periapsis altitude at 60-70°N. In this orbit the MLA ranged to Mercury from 29 March 2011 to 16 April 2012, densely sampling the north polar region in nadir mode northward to 83.5° N and sparsely in off-nadir mode at more northerly latitudes (Fig. 1A) (*1*). More than 4 million topographic and 2 million reflectance measurements were collected at latitudes greater than 65°N in the first year of mapping. Of 700 orbital profiles, 60 targeted latitudes higher than 84°N with off-nadir ranges, some yielding energy measurements and some not (fig. S1). Orbital geometry and power and thermal constraints precluded observations of many polar craters, and measureme nts of those that were accessible at oblique incidence returned noisier measurements than at nadir orientation.

A map of radar cross-section in the north polar region at S-band (12.6-cm wavelength) (*9*) (Fig. 1B) shows many regions of high backscatter cross-section; other such regions extend beyond the limits of the map to latitudes as low as 67°N. The polarization characteristics of these regions are suggestive of cold-trapped volatiles (*5*, *6*, *18*). These radar-bright (RB) features generally coincide with high-latitude, steep-walled craters of which the southern floors are permanently shadowed from direct sunlight because of Mercury's near-zero obliquity. The largest RB features lie north of 85° N, whereas the 108-km-diameter Prokofiev crater [previously given the informal name "K" (*18*)] has a crescent-shaped RB region behind its steep (17° slope) north-facing wall, just south of 85°N (Fig. 1B). With a depth-to-diameter ratio of 0.025, typical for a complex crater of this size, only a portion of its floor can lie in permanent shadow, consistent with the shape of the RB region. An unnamed 1.5-km-deep, 18-km-diameter crater "Z" lies on the central floor of Prokofiev and is RB. The 62-km-diameter crater Kandinsky (formerly "J") to the north has a nearly circular RB region (Fig. 1B). These and similar regions may now be subjected to illumination models that utilize detailed polar topography (*19*).

A plot of the maximum illumination flux over 10 solar days is shown in Fig. 1C. We modeled the primary shadowing of the finite disk of the Sun with the orbital and rotational geometry of Mercury following an earlier methodology (*20*). Zero flux corresponds to areas of near-permanent shadow that receive only scattered light. Mercury's orbital eccentricity and 3:2 spin–orbit resonance result in lower average solar flux near longitudes of 90° and 270°E. Shallow, degraded craters and craters lying near the 0° and 180°E longitudes of Mercury's equatorial "hot poles" have higher average illumination. Except for relatively fresh craters on the northern smooth plains (*1*), there are few RB features

along these azimuths south of 85°N.

The reflectance measurements binned at 1 × 1 km resolution are shown in Fig. 1D. The log-normally distributed quantity r_s has a mean of 0.17 ± 0.05, and 98% of returns have $r_s < 0.3$ (fig. S1). For comparison, the broadband geometric albedo of Mercury from space is 0.142 (*21*). About 7% of returns comprise a secondary "MLA-dark" (MD) mode distinguished by $r_s < 0.1$. This mode is seen in regions that are markedly darker than their surroundings. These regions coincide with areas where many received pulses do not trigger at the high threshold (fig. S2), although weak laser output, oblique incidence, steep terrain, and/or extreme range, as well as low reflectivity, can lead to poor signal recovery. The deficit of energy measurements in many MD regions indicates that the measured r_s values are upper bounds for surface albedoes that are lower by factors of 2–3 than their surroundings.

Many of the MD regions are associated with polar craters containing RB material (Fig. 2). The larger MD regions generally enclose the RB features. MD returns lie mainly within regions of very low peak illumination, although not necessarily permanent shadow. The reflectance is low over the southern floors and the northward-facing walls of virtually all craters at latitudes between 75° and 84°N. Darkening also occurs on some poleward-facing exterior rim slopes of craters in the otherwise smooth plains within the 320-km-diameter Goethe basin. Such darkening extends into regions that are partially illuminated.

The asymmetric distribution of MD regions with respect to terrain slope direction does not simply result from observing geometry, surface roughness, or the magnitude of the surface slope. The pulses returning from the MD portions are not noticeably wider or narrower than those from the illuminated portions, nor do equator-facing portions of the floor show lower reflectance. If surface slope or roughness were causing reduced energy return, the darker regions would have a circular outline. The correspondence of dark material with pole-facing slopes and the lack of such darkening in most craters southward of 70°N appears to rule out instrumental effects or observational geometry as a cause of the surficial darkening.

To assess the relationship between MLA-dark features, RB deposits, and illumination, we examined (*22*) 175 regions of low illumination identified as lying within craters varying in size from ~7 to 108 km in diameter (*23*) and from 65°N poleward (Table 1). All craters with RB deposits and sufficient MLA sampling show at least some MD features in their poleward facing portions. Of 128 RB craters with RB deposits, 96 contain collocated MD portions, whereas there are 28 additional craters with MD material that lack a corresponding RB signature. Two such craters (b5, f5) that are shown in Fig. 2 and fig. S3 are relatively pristine (> 1 km deep), so their interiors may not be visible to Earth-based radar. Twelve such craters are < 14 km in diameter. Those craters with MD material that lack a RB signature and are 14 km or larger in diameter are at latitudes south of 80°N. As with the RB regions, MLA-dark deposits are more prevalent near 90° and 270°E, longitudes that receive less average illumination as a result of Mercury's spin–orbit resonance and eccentric orbit, and in fresh craters on the smooth plains. At latitudes north of 75°N, 15 similar shadowed regions (putatively small craters) with neither a RB signature nor MD material are located mainly on an elevated area surrounding Purcell crater between longitudes 170° and 230°E. Radar coverage may be partially obscured by rough terrain in this sector, but the lack of RB features more likely has a thermal origin at these "hot pole" longitudes in locations where partial illumination might preclude stability of near-surface water ice, as illustrated in fig. S4.

Although the MLA-dark regions are more abundant and extensive than RB regions, there are at least nine areas within the largest RB regions at very high latitudes in which the MLA reflectances are optically bright. The nine craters hosting RB material, at latitudes between 82.5° and 88.5°N, have portions with $r_s > 0.3$ as well as areas that are anomalously dark or that return no reflectance measurements. The two most prominent such craters are north of 84.9°N latitude.

Craters Kandinsky and Prokofiev, for which high radar cross-sections suggest thick, near-surface ice deposits (*18*), are shown in Fig. 3. Their regions of permanent shadow (Fig. 1C) have many reflectance values in excess of 0.3 (pink or white symbols), especially along the southern portion of Prokofiev. Three profiles crossing the RB region are plotted along-track in Fig. 3B–D. Profile 3B grazed the uppermost kilometer of the crater wall and recorded no high-threshold detections in regions of shadow. Profile 3C passed 2 km into the interior along the north-facing wall and shows many strongly reflective returns (red symbols) up to the edges of the crater, where such returns dropped out for several seconds. Profile 3D reached portions of the crater floor that are in permanent shadow and recorded variable reflectance. These profiles are the only ones to date obtained over the shadowed interior of Prokofiev at the relatively small incidence angles (6°–7°) for which reflectance measurements are most reliable. Two profiles nearest to crater Z (Fig. 3A) also include returns with $r_s > 0.3$, as do several traversing crater Kandinsky to the north, but the measurements are noisier owing to incidence angles greater than 25°.

The observations of 1064-nm reflectance from laser altimetry thus fall into three categories: most are typical of Mercury reflectivity as a whole; a subset is much darker; and a smaller subset is substantially brighter. The association of MD regions with RB regions in near-permanent shadow suggests that a thin, radar-transparent layer of optically dark material overlies and surrounds the postulated polar ice deposits. If water ice were present in the ground as a matrix between mineral grains, it could lower the reflectance relative to dry ground but would sublimate rapidly and lose optical contrast if exposed to high temperatures. The presence of MD regions in many smaller craters without RB deposits, areas where scattered light raises average temperatures (*2*, *24*), indicates the presence of volatiles that are both darker than water ice and stable to higher temperatures.

The identification of optically bright regions associated with large RB features at the highest (>84.9°N) latitudes is consistent with the hypothesis that water ice is exposed at the surface in areas where surface temperatures are never sufficiently high for substantial loss by sublimation. The surface measurements are averages over footprints that are dozens of meters in extent and could represent a thin or unevenly distributed layer of optically bright material that has not been covered by dust or regolith. To the extent that MLA-bright and RB characteristics are sampling the same material, however, the associated deposits must have a thickness of at least several meters. The reflectance measurements presented here strongly suggest that one of the largest and deepest regions of permanent shadow in crater Prokofiev is a host for water ice deposits exposed at the surface.

The existence of these dark and bright surfaces and their association with topography indicates that their formation processes operated during geologically recent times and may be active on Mercury today. The rates of darkening and brightening must be higher than those for processes that act to homogenize surface reflectance, such as impact gardening. Were vertical mixing by impact gardening dominant at the meter scale, we would expect that the polar deposits would have reflectance values (and radar backscatter characteristics) more similar to those of surrounding terrain.

Detailed thermal models (*25*) suggest that surface temperatures in the majority of the high-latitude craters with RB deposits that MLA has observed to date are too warm to support persistent water ice at the surface, but the temperatures in their shadowed areas are compatible with the presence of surficial dark organic material. Modeled subsurface temperatures in these dark regions are permissive of stable water ice beneath a ~10-cm-thick layer of thermally insulating material. In contrast, thermal modeling of the bright areas is supportive of surface water ice. This interpretation of the surface reflectance at 1064 nm is fully consistent

with the radar results as well as with neutron spectroscopic measurements of Mercury's polar regions (*26*). The bright and dark areas can be ascribed collectively to the deposition of water and organic volatiles derived from the impacts of comets or volatile-rich asteroids on Mercury's surface and migrated to polar cold traps via thermally stimulated random walk (*27*–*29*).

References and Notes

1. M. T. Zuber *et al*., Topography of the northern hemisphere of Mercury from MESSENGER laser altimetry. *Science* **336**, 217 (2012). doi:10.1126/science.1218805 Medline
2. A. R. Vasavada, D. A. Paige, S. E. Wood, Near-surface temperatures on Mercury and the Moon and the stability of polar ice deposits. *Icarus* **141**, 179 (1999). doi:10.1006/icar.1999.6175
3. K. Watson, B. C. Murray, H. Brown, The behavior of volatiles on the lunar surface. *J. Geophys. Res.* **66**, 3033 (1961). doi:10.1029/JZ066i009p03033
4. J. R. Arnold, Ice in the lunar polar regions. *J. Geophys. Res.* **84**, 5659 (1979). doi:10.1029/JB084iB10p05659
5. M. A. Slade, B. J. Butler, D. O. Muhleman, Mercury radar imaging: evidence for polar ice. *Science* **258**, 635 (1992). doi:10.1126/science.258.5082.635 Medline
6. J. K. Harmon, M. A. Slade, Radar mapping of mercury: full-disk images and polar anomalies. *Science* **258**, 640 (1992). doi:10.1126/science.258.5082.640 Medline
7. B. J. Butler, D. O. Muhleman, M. A. Slade, Mercury: Full disk radar images, and the detection and stability of ice at the north pole. *J. Geophys. Res.* **98**, 15,003 (1993). doi:10.1029/93JE01581
8. G. J. Black, D. B. Campbell, J. K. Harmon, Radar measurements of Mercury's north pole at 70 cm wavelength. *Icarus* **209**, 224 (2010). doi:10.1016/j.icarus.2009.10.009
9. J. K. Harmon, M. A. Slade, M. S. Rice, Radar imagery of Mercury's putative polar ice: 1999–2005 Arecibo results. *Icarus* **211**, 37 (2011). doi:10.1016/j.icarus.2010.08.007
10. J. F. Cavanaugh *et al*., The Mercury Laser Altimeter instrument for the MESSENGER mission. *Space Sci. Rev.* **131**, 451 (2007). doi:10.1007/s11214-007-9273-4
11. The MLA is a time-of-flight laser rangefinder that uses direct detection and pulse-edge timing to determine precisely the range from the MESSENGER spacecraft to Mercury's surface. MLA's laser transmitter emits 6-ns-long pulses at an 8-Hz rate with 20 mJ of energy at a wavelength of 1064 nm. Return echoes are collected by an array of four refractive telescopes and are detected with a single silicon avalanche photodiode detector. The timing of laser pulses is measured with a set of time-to-digital converters linked to a crystal oscillator for which the frequency is monitored from Earth.
12. S. C. Solomon, R. L. McNutt, Jr., R. E. Gold, D. L. Domingue, MESSENGER mission overview. *Space Sci. Rev.* **131**, 3 (2007). doi:10.1007/s11214-007-9247-6
13. M. J. Talpe *et al*., Characterization of the morphometry of impact craters hosting polar deposits in Mercury's north polar region. *J. Geophys. Res.*, in press (2012). doi:10.1029/2012JE004155
14. G. B. Hansen, T. B. McCord, Amorphous and crystalline ice on the Galilean satellites: A balance between thermal and radiolytic processes. *J. Geophys. Res.* **109**, E01012 (2004). doi:10.1029/2003JE002149
15. The MLA measures the threshold crossing times of the received pulses at two discriminator voltages simultaneously, a low threshold for maximum sensitivity, and a threshold approximately twice as high to give four sample points of the received pulse waveform. A laser pulse may result in triggers at one or both thresholds or not at all. Ranging with low threshold detections is possible at ranges up to 1500 km, but steady returns that cross both the low and high thresholds are obtained mostly at altitudes less than ~600 km and with near-nadir (<20°) incidence. When a pulse is detected by a pair of discriminators, its energy and duration may be inferred from a model waveform that accounts for the dispersion in time of return pulses as a result of surface slope and/or roughness. To estimate the pulse energy we adopted a simple triangular model that fits the rising and falling edges of the trigger at each threshold. This model generates values nearly equal to a Gaussian model for well-constrained pulses. Energy is a nonlinear function of pulse timing measurements and tends to have a long-tailed or approximately lognormal distribution, as illustrated in the Supplementary Material.
16. C. S. Gardner, Ranging performance of satellite laser altimeters. *IEEE Trans. Geosci. Rem. Sens.* **30**, 1061 (1992). doi:10.1109/36.175341
17. The lidar link equation is $E_{rx} = E_{tx}\,\eta_r\,(A_r/R^2)\,(r_s/\pi)$ where E_{rx} is the received signal pulse energy, E_{tx} is the transmitted laser pulse energy, η_r is the receiver optics transmission, A_r is the receiver telescope aperture area, R is range, and r_s is the target surface reflectivity (relative to Lambertian). The ratio r_s of reflected energy to incoming energy (i.e., irradiance/solar flux, often simply written I/F) would be unity for a perfect diffusive reflector for which the transmitter and receiver orientation are perpendicular to the surface. Mercury's reflectivity at optical wavelengths normally lies in a range 0.08–0.12 (*30*–*32*), but because of the opposition effect (*33*) the average 1064-nm reflectance is approximately 50% higher, or about 0.17.
18. J. K. Harmon, P. J. Perillat, M. A. Slade, High-resolution radar imaging of Mercury's north pole. *Icarus* **149**, 1 (2001). doi:10.1006/icar.2000.6544
19. The topography derived from 700 MLA profiles (29 March 2011 to 1 May 2012) provides a near-complete topographic map of the northern hemisphere northward to 84°N at a resolution of 0.5 km. Craters Prokofiev and Kandinsky were sampled by several off-nadir profiles, from which radial averages of topography were constructed and used to fill in the unsampled interior after adding pseudo-random noise, with a root variance of 70 m, and decimating and interpolating with the 'blockmedian' and 'surface' programs of the Generic Mapping Tools (http://gmt.soest.hawaii.edu). We modeled the average and maximum illumination conditions over a Mercury day using an approach (*20*) developed to assess illumination conditions of polar regions of the Moon.
20. E. Mazarico, G. A. Neumann, M. T. Zuber, D. E. Smith, M. H. Torrence, Illumination conditions of the lunar polar regions using LOLA topography. *Icarus* **211**, 1066 (2011). doi:10.1016/j.icarus.2010.10.030
21. A. Mallama, D. Wang, R. A. Howard, Photometry of Mercury from SOHO/LASCO and Earth: The phase function from 2 to 170°. *Icarus* **155**, 253 (2002). doi:10.1006/icar.2001.6723
22. We selected 175 representative regions of interest from maps of permanent shadow derived from MLA topography, radar cross-section, and MLA-dark regions, as shown in the Supplementary Material. Because many craters are not resolved by MLA, we also selected craters with diameters ≥7 km from MESSENGER images. Smaller RB deposits were not considered because most appear from images to lie in small secondary craters, at the foot of poleward-facing scarps, or in rough terrain, and are inadequately sampled by MLA. The radar-bright deposits were mapped with a threshold of 0.075 in the MATLAB image processing toolbox, and correlated with craters identified in MLA topography and MESSENGER images. Labels assigned in uppercase are consistent with previous nomenclature (*15*); lowercase letters and numerals were assigned to provisional features. Regions with MLA energy measurements were classified as dark, normal, or bright/mixed according to their contrast in brightness with those of surround areas; gaps in high-threshold returns were also taken to indicate darker material. Bright regions are those for which more than half of the returns have $r_s > 0.3$.
23. Diameters of large craters were fit to the maximum MLA topographic contours of the rims, whereas the diameters of smaller craters were estimated from Mercury Dual Imaging System (MDIS) (*34*) image mosaics. Locations are less certain for smaller features inadequately sampled by MLA. Diameters of craters sampled ranged from 7 to 108 km, not including the 320-km-diameter Goethe basin. Not included are several degraded and partially flooded craters, such as a 133-km-diameter degraded crater that encloses Purcell but for which the relief does not create an area of permanent shadow.
24. D. A. Paige, S. E. Wood, A. R. Vasavada, The thermal stability of water ice at the poles of mercury. *Science* **258**, 643 (1992). doi:10.1126/science.258.5082.643 Medline
25. D. A. Paige *et al*., Thermal stability of volatiles in the north polar region of Mercury. *Science*, published online 29 November 2012 (10.1126/science.1231106).
26. D. J. Lawrence *et al*., Evidence for water ice near Mercury's north pole from MESSENGER Neutron Spectrometer measurements. *Science*, published online 29 November 2012 (10.1126/science.1229953).
27. B. J. Butler, The migration of volatiles on the surface of Mercury and the Moon. *J. Geophys. Res.* **102**, 19,283 (1997). doi:10.1029/97JE01347
28. J. A. Zhang, D. A. Paige, Cold-trapped organic compounds at the poles of the Moon and Mercury: Implications for origins. *Geophys. Res. Lett.* **36**, L16203 (2009). doi:10.1029/2009GL038614

29. J. A. Zhang, D. A. Paige, Correction to Cold-trapped organic compounds at the poles of the Moon and Mercury: Implications for origins. *Geophys. Res. Lett.* **37**, L03203 (2010). doi:10.1029/2009GL041806
30. T. B. McCord, J. B. Adams, Mercury: surface composition from the reflection spectrum. *Science* **178**, 745 (1972). doi:10.1126/science.178.4062.745 Medline
31. F. Vilas, Mercury: Absence of crystalline Fe^{2+} in the regolith. *Icarus* **64**, 133 (1985). doi:10.1016/0019-1035(85)90044-2
32. W. E. McClintock *et al*., Spectroscopic observations of Mercury's surface reflectance during MESSENGER's first Mercury flyby. *Science* **321**, 62 (2008). doi:10.1126/science.1159933 Medline
33. T. Gehrels, Photometric studies of asteroids. V: The light-curve and phase function of 20 Massalia. *Astrophys. J.* **123**, 331 (1956). doi:10.1086/146166
34. S. E. Hawkins, III *et al*., The Mercury Dual Imaging System on the MESSENGER spacecraft. *Space Sci. Rev.* **131**, 247 (2007). doi:10.1007/s11214-007-9266-3
35. N. L. Chabot *et al*., Craters hosting radar-bright deposits in Mercury's north polar region: Areas of persistent shadow determined from MESSENGER images. *J. Geophys. Res.*, in press (2012). doi:10.1029/2012JE004172

Acknowledgments: The MESSENGER project is supported by the NASA Discovery Program under contracts NAS5-97271 to The Johns Hopkins University Applied Physics Laboratory and NASW-00002 to the Carnegie Institution of Washington. We are grateful for the myriad of contributions from the MLA instrument and MESSENGER spacecraft teams and for comments by Paul Lucey and two anonymous referees that improved the manuscript.

Supplementary Materials
www.sciencemag.org/cgi/content/full/science.1229764/DC1
Supplementary Text
Figs. S1 to S5
Reference (*35*)

05 September 2012; accepted 14 November 2012
Published online 29 November 2012
10.1126/science.1229764

Table 1. Classification of 175 craters according to radar and optical characteristics of associated deposits.

Radar	MLA dark	MLA bright/mixed	MLA normal	MLA undetermined
Bright	96	9	0	24
Dark	28	0	15	3

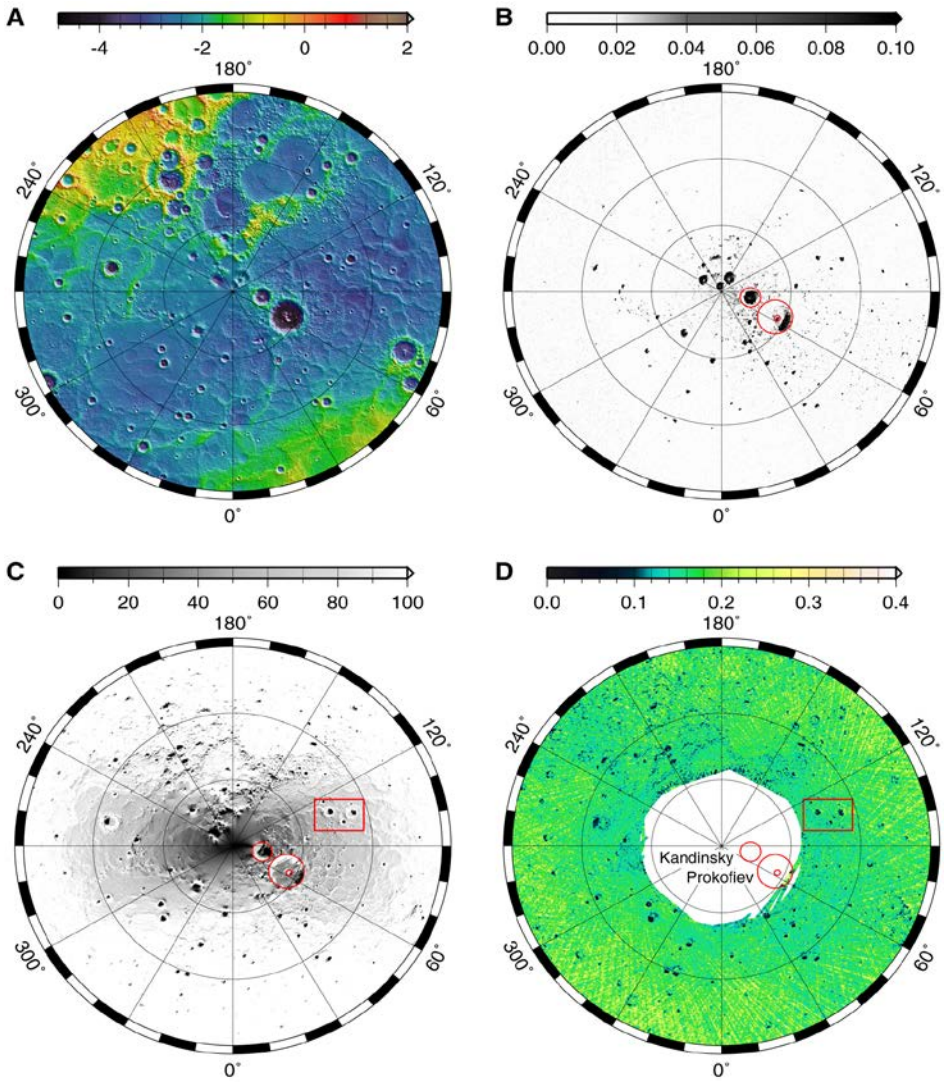

Fig. 1. Maps of topography, radar cross-section, solar illumination, and reflectance, in polar stereographic projection southward to 75°N. Kandinsky and Prokofiev craters are outlined in three of the four panels. (A) Topography (color scale in km) and shaded relief; the datum is a sphere of radius 2440 km. (B) Earth-based radar image (*9*) displayed as dimensionless radar cross-section per unit area. (C) Maximum incident solar flux over a 10-year period as a percentage of the solar constant at 1 AU from an illumination model. The red box outlines the region shown in Fig. 2. (D) 1064-nm bi-directional reflectance from MLA low- and high-threshold measurements in near-nadir directions, median-averaged in 1 km by 1 km bins. At latitudes poleward of 84°N, MLA obtained only a limited number of off-nadir profiles, and the projected reflectance data in this region are interpolated by a nearest-neighbor weighted average only within 2 km of data whose incidence angles were less than 10°.

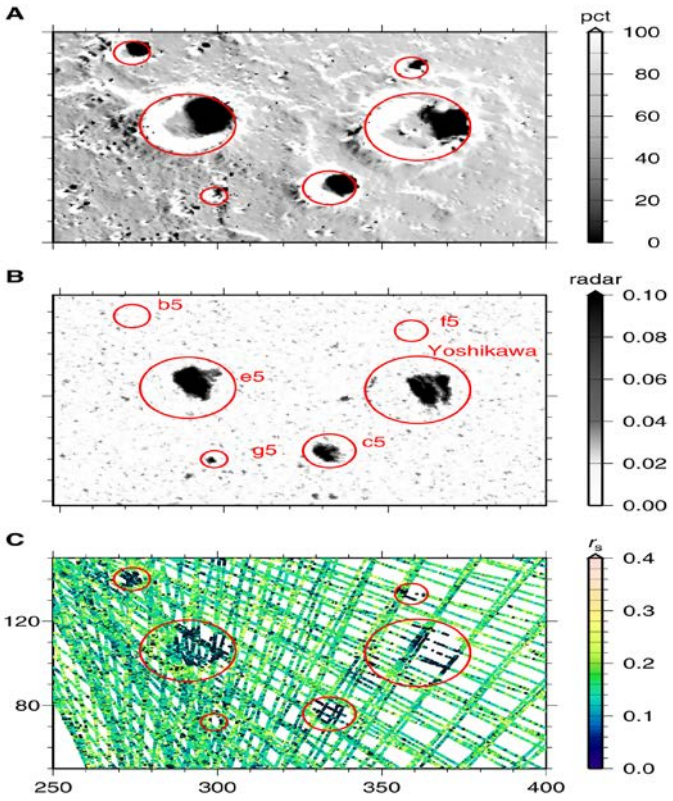

Fig. 2. Regional view of the area outlined in Fig. 1, in polar stereographic projection. Red circles show the outlines of six craters. (A) Maximum incident solar flux, as a percentage of the solar constant at 1 AU. (B) Radar cross-section per unit area. The projected radar map (*9*) has been shifted by 2 km to achieve optimal registration with the MLA-based maps. Regions of interest (*22*) are labeled. (C) MLA reflectance (colored dots).

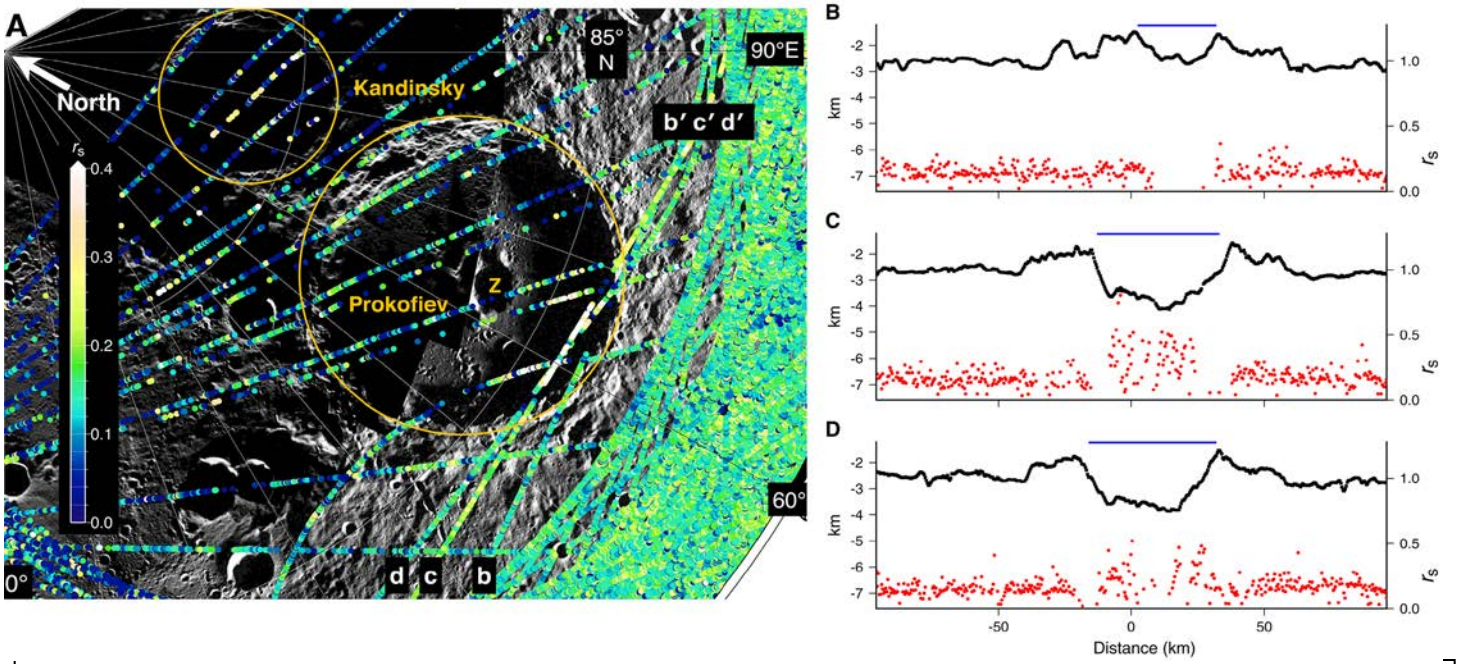

Fig. 3. (A) MLA reflectance measurements (colored dots) of the north polar region from longitude 0° to 90° E and latitude 82.5° to 90° N. Background is a mosaic of MDIS (*34*) frames at different illumination geometries and has a nonlinear contrast stretch for visibility. Three profiles through Prokofiev (b-b', c-c', d-d') were acquired at near-nadir orientation. Profiles through Kandinsky were acquired at ~30° off-nadir orientation. (B,C,D) Profiles of height (black) and reflectance (red dots) through Prokofiev acquired on 22-24 March 2012 starting at 0308 UTC on each day, at a 5-7° nadir angle. Vertical exaggeration is 10:1. The profiles are centered at longitude 60°E and traverse the poleward-facing wall of Prokofiev crater in an approximately west-to-east direction. The blue lines show the modeled extent of low average solar flux (< 50 W m^{-2} or < 0.04 of terrestrial)